This article has been accepted for publication in IEEE Transactions on Ultrasonics, Ferroelectrics, and Frequency Control. This is the author's version which has not been fully edited and content may change prior to final publication. Citation information: DOI 10.1109/TUFFC.2025.3596780

A Fully Populated Transrectal Array for Boiling Histotripsy Ablation of the Prostate

Pavel B. Rosnitskiy, Gilles P.L. Thomas, Gerald L. Lee, Vera A. Khokhlova,
Oleg A. Sapozhnikov, George R. Schade, Kyle P. Morrison, Francisco Chavez, and
Tatiana D. Khokhlova

***Abstract*—Endorectal ultrasound (US)-guided thermal ablation of prostate cancer using high-intensity focused ultrasound (HIFU) is a widely used focal intervention. While generally safe and effective, it is not without challenges associated with heat diffusion and prefocal heating, which has spurred interest towards non-thermal, mechanical HIFU ablation regimes. Another challenge is the necessity to mechanically translate the HIFU transducer – commonly single-element or annular array – for volumetric treatments, which results in target shifts and transducer position readjustment. 2-D arrays would address this problem, but their design is challenging in a small form-factor. The element pattern must be tightly packed and aperiodic to maximize active surface area and to suppress grating lobes, respectively. Here, we report on the design, fabrication, and performance evaluation of a 1.5-MHz 128-element transrectal HIFU array driven by Verasonics system capable of mechanical tissue ablation *via* boiling histotripsy (BH) under real-time coaxial US imaging guidance. A recently developed method for designing randomized, fully-populated mosaic arrays was used to create the element pattern. The measured focus steering ranges of the fabricated array were 26 mm axially and 12 mm laterally in the BH regime, with driving voltage compensation by less than 43% and no grating lobe formation. Stress tests with a 5-element prototype confirmed safe operating voltage of 850 V peak-to-peak, corresponding to the acoustic intensity of 542 W/cm^2 at the array surface. The array integrated with a 128-element US imaging probe driven by the same Verasonics system was successfully used to produce volumetric BH lesions in polyacrylamide tissue-mimicking phantoms.**

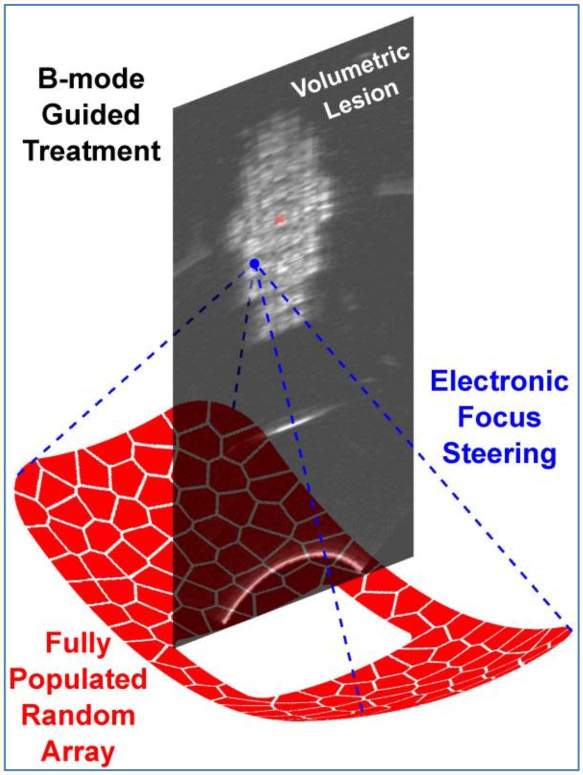

***Index Terms*— Multi-element array, high-intensity focused ultrasound (HIFU), prostate, boiling histotripsy, tight packing, focus steering, nonlinear waves**

I. INTRODUCTION

One of the most promising applications of high-intensity focused ultrasound (HIFU) is non-invasive (incisionless) ablation of prostate cancer (PCa) as an alternative to the current first-line treatments such as radical prostatectomy and radiation [1, 2, 3, 4]. HIFU approach utilizes transrectal probes that generate high-intensity focused ultrasound beam propagating through the rectal wall to the target region of the prostate (Fig. 1(a)). This leads to rapid localized heating and subsequent coagulative necrosis of the targeted tissue. This technology has been implemented in two commercial systems that have been successfully used in clinical practice for over a decade: Focal One® (EDAP, Vaulx-en-Velin, France) and Sonablate® HIFU (Sonablate Corp., Charlotte, NC, USA) [2, 3, 4, 5].

The Focal One® system includes a compact annular array of spherically focused elements arranged in a “spoon” shape with a circular central opening for the co-axial US imaging probe, as seen in an illustration of such a transducer array in Fig. 1(b). This element arrangement enables electronic focus steering along the HIFU axis z [6]. However, this pattern does not allow movement of the focus in the transverse x and y directions, which is instead performed *via* mechanical probe translation along and rotation around y axis. Such mechanical movement

---

This work was supported in by NIH R01CA258581 (Corresponding author: Pavel B. Rosnitskiy). Please see the Acknowledgment section of this article for the author affiliations.

Highlights

- **A novel design for a fully populated 128-element transrectal array for mechanical prostate ablation *via* boiling histotripsy method under B-mode guidance was proposed.**
- **The complete design process, from numerical simulations to optimize the array parameters to phantom testing of the manufactured array in tissue-mimicking polyacrylamide gel is presented.**
- **Phantom tests confirmed safe and efficient focus steering over a 25.5 mm along and 12 mm transverse the array axis with sufficient power reserve for *in vivo* use.**

of the HIFU probe during treatment is associated with decreased ablation rates, can lead to trapping of gas bubbles between the probe cover and the rectal wall, and causes shifting and deformation of the prostate. These challenges necessitate transducer position readjustment, which increases procedure duration, compromises targeting accuracy and introduces operator dependence. The capability of electronic focus steering in those directions, with the transducer remaining stationary, would thus be beneficial for both treatment efficiency, precision, and reliability. Steering in the xz plane (Fig. 1(b), semitransparent region) is of particular interest, as it corresponds to the US imaging plane. This highlights the need for a transducer with a two-dimensional (2-D) multi-element pattern and three-dimensional (3-D) focus steering capabilities.

The design of a 2-D transrectal array is particularly challenging due to the critical requirement for a small form factor, which necessitates densely packed elements to maximize the active surface area and power output. One straightforward way of achieving such a pattern of elements with equal surface area is to divide the array into a regular grid of rectangular elements (Fig. 1(c)). However, periodic distribution of the elements with spacing comparable to the HIFU wavelength leads to the formation of high-amplitude grating lobes in the HIFU field when the focus is electronically steered [7]. Thus, the key challenge is the design of an irregular, densely populated pattern of elements of equal area to reduce grating lobes.

Another set of challenges in transrectal HIFU treatment of the prostate is related to the thermal ablation mechanism. The treatments are limited by thermal diffusion from relatively slow heating, pre-focal heating which causes edema, and tissue attenuation which limits the ability to effectively heat the anterior prostate [8]. Furthermore, vapor bubbles that form in ablated tissue are frequently persistent and result in shadowing of the posterior areas on US images, forcing the operator to pause the treatment for their dissolution. Finally, B-mode evaluation of purely thermal treatment outcomes provides only minimal real-time feedback.

One potential solution to these challenges is using non-thermal, mechanical tissue ablation, i.e., histotripsy. Histotripsy mechanically liquefies tissue through bubble activity induced by short high-amplitude HIFU pulses delivered at low duty cycle [9, 10, 11, 12]. Since histotripsy techniques rely on bubble formation in the target region during the procedure, the resulting hyperechogenicity can precisely highlight the treatment area in B-mode images, while treatment completion can be confirmed by hypoechoic region of the liquefied tissue [12]. Several histotripsy regimes have been identified over the past two decades and differ primarily in the pulse duration (microseconds to milliseconds) and necessary HIFU focal pressures (higher to lower, respectively) [12, 13].

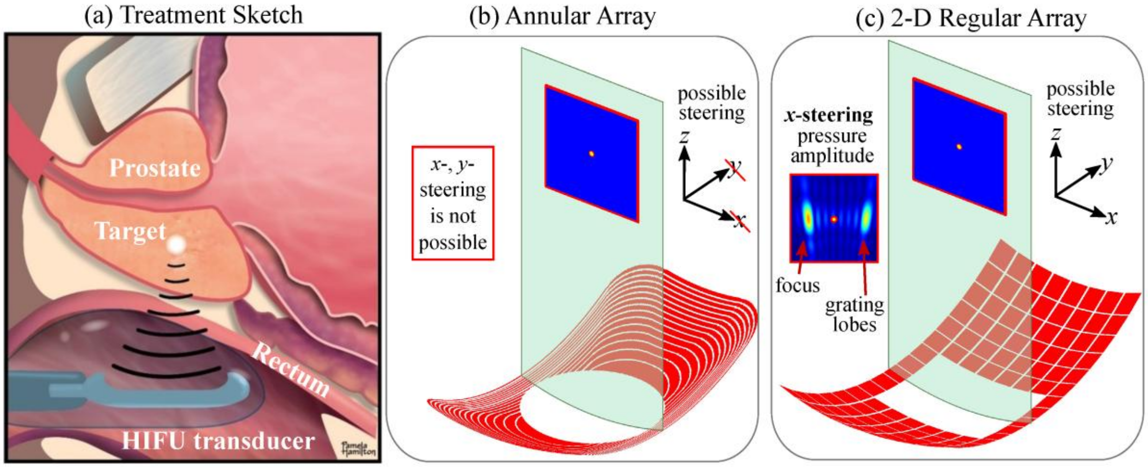

Fig. 1. Illustration of challenges in thermal HIFU ablation of prostate cancer. (a) A sketch of transrectal thermal HIFU ablation of the prostate. (b) Sketch of an annular HIFU array similar to those used in Focal One® systems. A semi-transparent rectangle represents the imaging plane of the coaxial US imaging probe. A contour within the imaging plane indicates the region of interest (ROI) of the array's acoustic field, while the circular marker denotes the center of curvature of the array. (c) Sketch of an array with a 2-D regular pattern of elements. A pressure amplitude field sketch in the ROI is shown for a case where the focus is electronically steered along x axis to illustrate the formation of grating lobes.

Historically, the first successful histotripsy treatments of the prostate utilized the shock-scattering histotripsy regime, (10 – 20 microsecond long pulses, 1% duty cycle) and were performed transabdominally in the canine model inclduing in the ACE-1 prostate cancer model [9, 14, 15]. However, a subsequent clinical trial of a transperineal histotripsy device in benign prostate hyperplasia (BPH) patients demonstrated no long-term benefit, suggesting inadequacy of transperineal acoustic window for effective mechanical ablation [16].

Another histotripsy regime – boiling histotripsy (BH) – utilizes millisecond-long pulses with shock fronts to repeatedly create a vapor bubble at the focus. This bubble interacts with the remaining incident shock fronts of the pulse, enabling mechanical tissue ablation without discernable thermal effects [11]. Due to lower power requirements for BH, transducer miniaturization is more feasible compared to shock-scattering histotripsy, making the transrectal approach possible [12, 17]. This was confirmed in a series of studies in which a 2-MHz single-element transrectal BH transducer was manufactured, and the feasibility of prostate BH was demonstrated in an *in vivo* canine model [18, 19, 20].

BH has also shown strong potential for ablating human prostate tissue. A series of *ex vivo* studies conducted in N=24 human autopsy samples with a wide range of elastic properties (stiffness) demonstrated successful ablation of benign prostatic hyperplasia (BPH) and a case of prostate adenocarcinoma [18, 21, 22]. A comparative study further demonstrated that BH protocols achieve 5–10 times faster ablation rates compared to protocols with microseconds-long pulses in *ex vivo* human prostate tissue [23].

An important next step in improving the transrectal BH ablation systems is the development of a 2-D multi-element array design to enable 3-D focus steering. Because BH requires high pulse average output power, it is important to maximize the active surface area by ensuring that the array is fully populated and matching the shape of the central opening to that of the US imaging probe (usually rectangular, Fig.1(c)).

The goal of this work was to design such a fully populated 2-D array for US-guided transrectal BH satisfying the requirements presented above and to evaluate its performance in tissue-mimicking phantoms. A novel method for designing randomized fully populated arrays – previously developed by the authors – was adapted for this case of a rectangular aperture and a rectangular opening [24, 25, 26]. The process included four stages: (1) numerical simulations to determine optimal device parameters in reaching the required steering range and output levels; (2) destructive testing with a specifically fabricated subset of elements to identify the safe range of their operation and potential modes of failure; (3) hydrophone-based characterization of the pressure field of the fabricated array in linear and nonlinear regimes; (4) volumetric BH exposures of a tissue-mimicking gel phantom under B-mode US guidance.

II. Materials and Methods

A. Selection of the Transducer Array Design Parameters

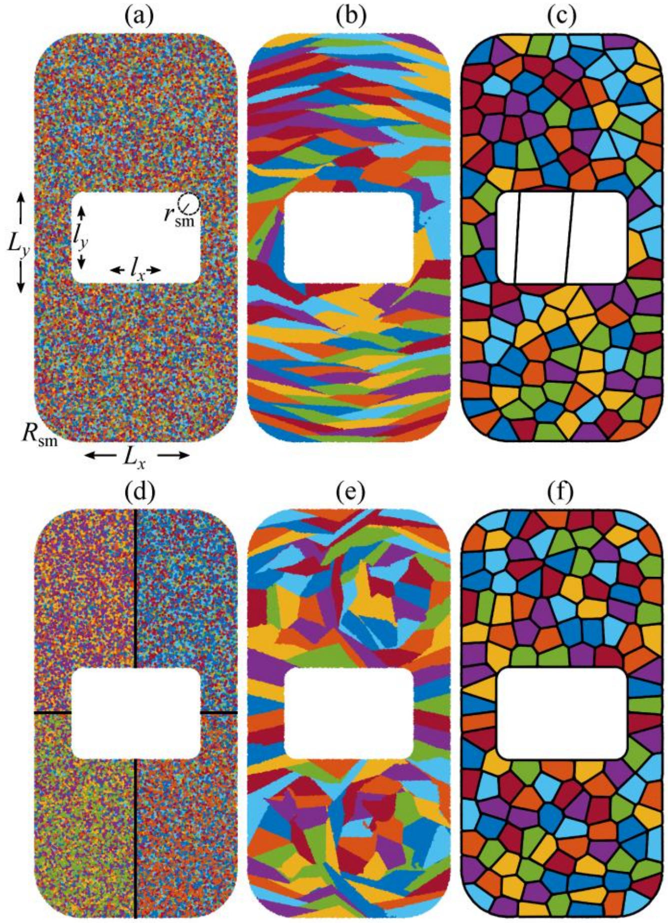

Fig. 2. Illustration of the capacity-constrained tessellation as an iterative point-clouds separation process for designing a transrectal BH array. The top row (a – c) shows three key iterations of the process for point clouds randomly mixed over the array's surface: (a) the completely blended state (iteration 0), (b) the beginning of separation (iteration 1), and (c) the completion of separation. Solid line contours outline the final tessellation cells. The bottom row (d – f) illustrates the same process for another initial state, where point clouds are generated in separate array quarters to prevent the breakage of tessellation cells into two parts.

The relevant BH-array design parameters include the radius of curvature of the spherical surface F, the size of the active surface in the x and y directions (referred to as "width" and "length", $L_x \times L_y$), the opening size ($l_x \times l_y$), the smoothing radii of the outer corners of the array aperture $R_{\rm sm}$, the inner corners of the opening $r_{\rm sm}$, the operating frequency f, the number of elements N, the element pattern, and the kerf h between the elements (Fig. 2(a)).

Another important parameter of a HIFU transducer is the F-number, which is defined as the ratio of the focal length of the transducer to its aperture. This parameter characterizes the focusing angle of the transducer. Rectangular transducers have therefore two F-number values along the x- and y-directions: $F_\#^x = F/L_x$ and $F_\#^y = F/L_y$. For the transducer geometry considered in this study, $L_y > L_x$, so it is convenient to define $F_\#^x$ as the F-number of the "weakly focused" side and $F_\#^y$ as the F-number of the "strongly focused" side (Fig. 2(a)). It has been previously shown that focal pressures corresponding to specific levels of nonlinear waveform distortion (critical to BH) are determined by the transducer F-number [27]. Specifically, for rectangular apertures, it is primarily determined by the F-number of the strongly focused side, $F_\#^y$ [28].

Some of the design parameters were determined based on the

This article has been accepted for publication in IEEE Transactions on Ultrasonics, Ferroelectrics, and Frequency Control. This is the author's version which has not been fully edited and content may change prior to final publication. Citation information: DOI 10.1109/TUFFC.2025.3596780

practical limitations of the driving electronics, anatomical limitations for transrectal applications, and previous studies on HIFU in the prostate. They were also informed by the parameters of a 2-MHz single-element transrectal BH transducer used in our previous prostate BH studies [29, 19, 20]. This transducer had a similar shape with the radius of curvature of 40 mm, a width and length of 30 × 50 mm, respectively, a circular central opening diameter of 23 mm, and F-numbers of $F_{\#}^{x} = 1.3$ and $F_{\#}^{y} = 0.8$.

For the current transducer, a greater radius of curvature, $F = 52$ mm, was selected to enlarge the treatment envelope and enable access to deeper tumors. This value is also consistent with those used in clinical transrectal HIFU systems, such as Focal One® (EDAP, Vaulx-en-Velin, France) [5].

The transducer width was dictated by the feasibility of transrectal use, and was selected based on practical clinical recommendations to not exceed 40 mm. Given the space required for the array housing, the width of the active surface was chosen as $L_x = 31$ mm. Similarly, the smoothing radius of the array aperture, $R_{\mathrm{sm}} = 7$ mm, was selected based on the existing devices [5]. The height of the array was set to $L_y = 63$ mm to achieve the same F-number, $F_{\#}^{y} = 0.8$, for the strongly focused side as the previously used single-element BH transducer, thereby ensuring a similar nonlinear field at the focus.

The size of the opening, $l_x = 21$ mm by $l_y = 15$ mm, and its smoothing radius, $r_{\mathrm{sm}} = 2$ mm, were chosen to accommodate the custom-made micro-convex 128-element imaging probe (VERMON SA, Tours, France) for treatment guidance.

The number of BH-array elements, $N = 128$, was selected to ensure compatibility with the 4-board Verasonics Vantage system with a HIFU option and custom capacitor bank (Verasonics Inc., Kirkland, WA, USA). Out of the 256 overall channels, half were planned for the 128-element HIFU array and the other half – for the 128-element US imaging probe. The fully populated 128-element pattern is described in Section II-B.

The kerf between the elements, $h = 0.4$ mm, was determined by the technological limits of the array manufacturing process. This kerf was necessary to avoid electrical breakdown between neighboring elements operating out of phase [24].

The operating frequency was considered in the range of $f = 1.5$ MHz to 2 MHz. Both frequencies have been successfully used in previous prostate BH studies [19, 20, 30]. The lower frequency of 1.5 MHz is known to produce larger lesions and therefore higher ablation rate as well as to improve focus steering capabilities [31]. Conversely, the higher frequency of 2 MHz offers the advantage of a higher focal gain, and the shock is formed at a lower driving voltage level.

Prior to the fabrication of the 128-element transducer, a 5-element prototype array made from the same lead zirconate titanate (PZT-4) piezoelectric material was manufactured for destructive testing in a high-power regime to assess the reliability of the selected element size and kerf. Details of these tests are provided in Section II-D.

B. Fully Populated Array Design

The fully populated design of the array was based on capacity-constrained tessellation (CCT), which was initially introduced for computer graphics applications [32]. This tessellation method was adapted in our prior work to design spherically focused bowl-shaped HIFU arrays with a randomized, fully populated pattern of elements of equal area [24, 25]. Since the design procedure was detailed in depth previously, here we only provide a qualitative description. Fig. 2 illustrates the implementation of the algorithm.

First, a large number of sampling points was randomly generated on the surface of the array according to a uniform probability distribution. Second, all points were divided into N randomly mixed sets of points – referred to as point clouds – each containing an equal number, M, of points (Fig. 2(a)). For example, the case where $N = 128$ and $M = 1000$ is shown.

The second stage of the algorithm can be described as the "separation" of N portions of various immiscible liquids, where each portion contains M sampling points mixed in a "container" shaped like a spherical shell. This separation process is implemented iteratively by swapping points between point clouds based on a specific metric that identifies pairs of points to be exchanged, as detailed in [24]. An example of the distribution of point clouds after the first iteration, $S = 1$, is shown in Fig. 2(b).

This process included "limited relaxation", which fixed the position of the center of mass of each point cloud at a specified iteration, S_0. Beyond this iteration, the separation process continued with the center of mass of each cloud remaining stable. A detailed explanation of this algorithm benefits is provided in [25]. Limited relaxation has been shown to increase the level of non-periodicity in the final element pattern and suppress the grating lobes. Therefore, the limited relaxation option, with a limiting iteration of $S_0 = 4$, was used for the current example.

The final iteration, with all point clouds separated, is shown in Fig. 2(c), forming the elements of the fully populated array. Since the number of uniformly distributed points within each element is proportional to a consistent, unbiased estimate of its area, the areas of all elements are equal in the limit of a large number of points, M. Thus, the desired fully populated pattern is achieved. However, one drawback of this design becomes evident for arrays with a wide opening in the x-direction: separate point clouds adjacent to opposite sides of the opening may cause separation of the corresponding array elements into two parts. An example of such an element is shown in Fig. 2(c). A solid contour outlining the rim of the element's point cloud passes through the central opening, as the element is split into two parts on either side of the opening.

To address this issue, a modified tessellation method was proposed and applied as follows. The initially mixed point clouds were generated independently within the four quadrants of the array aperture (Fig. 2(d)). In this configuration, point clouds located on the opposite sides of the opening remained "unmixed," preventing the separation process from dividing any cloud into two parts. The subsequent separation process proceeded in the same manner as in the original algorithm. The point clouds after the first and final iterations are shown in Figs. 2(e, f).

This article has been accepted for publication in IEEE Transactions on Ultrasonics, Ferroelectrics, and Frequency Control. This is the author's version which has not been fully edited and content may change prior to final publication. Citation information: DOI 10.1109/TUFFC.2025.3596780

To transition from a discrete representation of the point clouds to a continuous distribution of elements, rims around the outer points of each cloud were traced (Fig. 2(f), solid lines). The final tessellation parameters were $N = 128$, $M = 10^5$, $S_0 = 4$. A large value of M was chosen to ensure a small variation in the areas Σ_{el} of the elements, which does not exceed 1% [24]. Five hundred different random generations of the initial points were performed to create a statistical ensemble of arrays with varying random element patterns but identical geometric parameters. The array with the best performance was selected from this ensemble. The number 500 was chosen in accordance with a previous study on fully populated arrays, which demonstrated that this sample size is sufficient to obtain a representative statistical ensemble [25].

C. *Field Simulation and Array Selection*

Multiparametric modeling of the pressure field of each array from the ensemble was performed using an open-access xDDx toolbox, available from https://github.com/pavrosni/xDDx/releases. One of the capabilities of the Simulation part of that toolbox is the simulation of 3-D pressure fields of transducers with nonuniform distribution of vibrational velocity (amplitude and/or phase) over the active surface in a continuous wave (CW) regime [33]. The simulation algorithm is based on the Rayleigh integral, implemented using parallel computations on graphic processing units (GPUs), which allows for fast simulations for multiple transducer cases considered in this study. Simulations were performed assuming the propagation medium to be water with the sound speed of $c_0 = 1500$ m/s and the density of $\rho_0 = 1000$ kg/m^3.

The first set of simulations aimed to select the array with the largest focus steering range in z direction. This parameter is one of the most critical in practical applications because mechanical movement of the array in that direction is the most restricted. According to the "efficiency" and "safety" criteria from [34] and [35], the allowable steering range was defined as the range where the pressure amplitude at the shifted focus is higher than 70% of the maximum achievable value, and the steering is considered safe if the pressure amplitude of the grating lobes is less than 30% of the focal amplitude. These criteria assumed that the focal pressure losses could be compensated by increasing the pressure p_0 at the surface of the transducer, while maintaining the grating lobe level below 30% would ensure safety even with this pressure increase. Here, $p_0 = \rho_0 c_0 v_0$ is the characteristic initial pressure at the surface of the array element, where v_0 is the normal vibrational velocity amplitude of the element surface. Specifically, to compensate for a 70% reduction in focal pressure in a linear propagation case, the corresponding increase in p_0 would be 1/0.7 = 1.43, or by 43%. Note that in practice, since the characteristic initial pressure at the surface of the element is proportional to the electrical voltage applied to it, this 43% increase in p_0 is equivalent to a 43% increase in the driving voltage [22].

The allowable steering range was determined for each array in the ensemble by setting the phases at the elements to place the focus in the range of z_F from 35 mm to 65 mm with a step of 1.5 mm (21 positions). The range of positions Δz_F that fulfilled both the "efficiency" and "safety" criteria was then identified. As a result, a total of 500×21 field simulations were performed.

According to the input data format of the toolbox, each of the 500 array models was discretized on a Cartesian grid projected onto the spherical surface of the array with x- and y-steps of 0.1 mm. Pixels corresponding to the array elements were assigned amplitude and phase values calculated for each steering position, while pixels in the kerfs were assigned zero amplitude and phase. Simulations were performed for an operating frequency of 1.5 MHz.

Once the array with the widest steering range Δz_F was selected, more detailed field simulations were performed. Linear simulations of the pressure field in the vicinity of the center of curvature of the array were conducted at frequencies of 1.5 MHz and 2 MHz to evaluate whether the focal gain was sufficient to attain BH conditions. The lowest operating frequency satisfying those conditions was selected.

The steering range calculations were subsequently performed for the selected frequency in the zx- and zy-axial planes. These calculations considered focus positions ranging from –7 mm to 7 mm in the x- and y-directions (with a step of 0.25 mm) and from 35 mm to 65 mm in the z-direction (with a step of 0.5 mm).

Finally, the array field was simulated at the selected frequency in 3-D rectangular regions for seven focus positions: ($x_F = 0$, $y_F = 0$, $z_F = F$), ($x_F = \pm 5.5$ mm, $y_F = 0$, $z_F = F$), ($x_F = 0$, $y_F = \pm 6.6$ mm, $z_F = F$), ($x_F = 0$, $y_F = 0$, $z_F = 35.6$ mm), and ($x_F = 0$, $y_F = 0$, $z_F = 63.3$ mm). The first focus position corresponded to the center of curvature of the array, while the others were located at the x-, y-, and z-boundaries of the allowable steering range, as described above. The simulation grid spanned from –15 mm to 15 mm in the x- and y-directions and from 35 mm to 65 mm in the z-direction, with a step size of 0.1 mm in all directions resulting in $201 \times 201 \times 301$ simulation points. The simulated field was subsequently compared to the field of the fabricated array reconstructed from acoustic holography measurements to evaluate the fidelity of the build to the design. The acoustic holography method (described in Section II-E) involved hydrophone measurements of the 2-D pressure waveform distribution in a transverse plane in front of the transducer, followed by numerical forward and backward projection of the field [33]. To provide a quantitative comparison, the vibrational velocity v_0 at the surface of the simulated array was selected in a way that ensures the same total acoustic power $W_0 = \rho_0 c_0 v_0^2 N \Sigma_{\mathrm{el}} / 2$ as one of the CW components of the measured transient hologram W_{holo} at the selected operating frequency: $v_o = \sqrt{2W_{holo} / \rho_0 c_0 N \Sigma_{\mathrm{el}}}$. The details of holography measurements and holography-based power calculations are provided in Section II-E.

D. *Destructive Testing of a 5-element prototype*

Both the prototype 5-element array for destructive testing and the full 128-element probe were fabricated by Sonic Concepts Inc (Bothell, WA, USA). The same piezoelectric element material (PZT-4) and water-jet dicing technology were used for the prototype as those for the final array. The 5-element prototype consisted of a sub-group of elements from the final mosaic pattern selected in Section II-C. A 1/4 lambda carbon composite matching layer was bonded onto the diced PZT. The prototype elements were diced from a small spherically focused disc (20 mm diameter, 64 mm radius of curvature) integrated into a housing that was waterproof on the front to facilitate immersion of the transducer face into degassed, deionized water for testing. The back of the transducer was open, enabling visual observation of electric breakdown and temperature measurements (Fig. 3(a)).

Each element of the prototype array was driven independently using a custom-built class D amplifier *via* a custom matching network [36]. Since the real part of the impedance was close to 60 Ohms, a series inductor was selected to cancel the imaginary component of the impedance at 2 MHz. The inductor was chosen to be compact, shielded, and capable of handling the required current and voltage without saturation.

The elements were driven with different phase delays, as illustrated in Fig. 3(a). The phases of elements 1 and 3 were set to zero to test mechanical crosstalk between the elements working in phase, while elements 2 and 4 were driven with phase shifts of π to increase the probability of electrical breakdown between the pairs 1–2, 2–3, 3–4, working with the opposite polarity. An average phase shift of $\pi/2$ was set for element 5.

In the first set of measurements, the vibration pattern of the prototype was characterized with transient acoustic holography described in detail in Section II-E [37, 33, 38]. The second set of measurements consisted of destructive testing performed as follows. The transducer was driven in a typical BH pulsing regime (10 ms-long pulses, a PRF of 1 Hz) with gradually increasing the driving voltage at the elements within the range of 100–830 volts peak-to-peak (V_{pp}) with a step of 50 V. The transducer operated for at least 5 minutes at each level. The maximum element driving voltage of 830 V_{pp} corresponded to an output voltage of 90 V (10 V higher than the system's nominal maximum voltage) by the power modified Verasonics Vantage system).

The temperature of the active surface was monitored using an Etekcity LaserGrip 774 (Etekcity, Tustin, CA, USA) infrared (IR) thermometer, while electrical breakdown occurrence was visually observed from the back side of the transducer.

After identifying the failure mode of the transducer, the device was improved, and all measurements mentioned in this section were repeated to rule out post-failure damage.

E. Acoustic Holography Measurements

Transient acoustic holography was performed for the 5-element prototype and the fabricated 128-element array to evaluate of the fidelity of the element pattern to the design, the amount of mechanical crosstalk between elements and electroacoustic conversion efficiency across the available frequency range. A hologram measurement consisted of a 2-D planar hydrophone scan of the transient pressure field of the transducer in the plane perpendicular to the transducer's acoustic axis (z-axis) [37, 38].

The hydrophone measurements were conducted in a tank filled with degassed and deionized water. An HGL-0085 capsule hydrophone with an AH-2020 preamplifier set at 20 dB gain (Onda Corp., Sunnyvale, CA) was attached to a 3-D positioning system (Velmex Inc., Bloomfield, NY). The 2-D planar field scans were performed using a custom LabVIEW program (National Instruments Corp., Austin, TX) that controlled the movement of the hydrophone over a rectangular grid and the acquisition of the hydrophone signals at each grid node using a 14-bit digitizer at a sampling rate of 80 MHz (Gage Razor 14, DynamicSignals LLC, Lockport, IL, USA).

For the prototype transducer, the elements of the array were excited with 3-cycle pulses at 2 MHz with a pulse repetition frequency (PRF) of 5 Hz, and 4 V_{pp} voltage. The hologram xy grid consisted of 123×123 nodes with a step size of 0.25 mm and positioned at approximately z=34 mm from the transducer surface. For the 128-element transducer, 3-cycle pulses with similar parameters were used at a 1.5 MHz central frequency. Two holograms were acquired: one with all elements driven with the same phases to provide focusing at the center of curvature of the array ($x_F = 0$, $y_F = 0$, $z_F = F$), and another with the phases set to steer the focus laterally in the imaging plane ($x_F = 5.5$ mm, $y_F = 0$, $z_F = F$). The array was driven by the power-enhanced Verasonics Vantage system (Section II-A). The hologram xy grid consisted of 111×181 nodes with a step of 0.3 mm and positioned at approximately z = 30 mm.

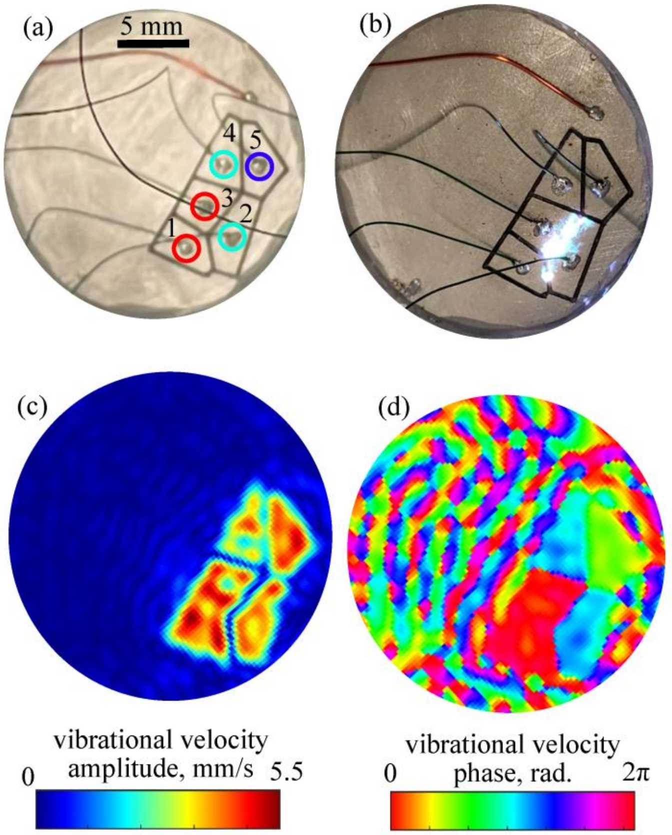

Fig. 3. (a) A photo of the back side of the 5-element prototype array. The elements are numbered from 1 to 5, and circles of different colors indicate the phase delays applied to the elements. Elements 1 and 3 were set to zero phase delay, elements 2 and 4 to a phase delay of π, and element 5 to a phase delay of $\pi/2$. (b) A photo showing an arcing spark caused by electrical breakdown between elements with opposite phases. (c) and (d) Vibrational velocity amplitude and phase in a low-amplitude 2-MHz CW regime, reconstructed at the surface of the prototype using the acoustic holography method.

This article has been accepted for publication in IEEE Transactions on Ultrasonics, Ferroelectrics, and Frequency Control. This is the author's version which has not been fully edited and content may change prior to final publication. Citation information: DOI 10.1109/TUFFC.2025.3596780

Post-processing of the holograms, which included alignment, forward projection to obtain 3D pressure field and backward projection to reconstruct the vibrational velocity pattern at the array surface, was performed using the Holography Part of the xDDx toolbox [33]. Back-projection was performed in two regimes: transient and single-frequency at the central frequency of each transducer. The transient regime is useful for revealing small-scale defects of the radiating surface, while the single-frequency regime demonstrates performance of the array for BH treatment protocols that include 10^3 – 10^4 cycles of the central frequency and may be considered quasi-CW [13]. To determine the electroacoustic efficiency of each array the acoustic power of the holograms at the respective central frequencies was determined using xDDx Power Spectrum Tool [39], and the electric power was calculated from the corresponding voltage waveforms and electrical impedances of the elements. The tool is based on the angular spectrum method for power calculation in a planar scan, detailed in [40].

F. Nonlinear Focal Waveform Measurements

The focal waveforms of the 128-element array in nonlinear regime relevant to BH were measured in water using a fiber-optic probe hydrophone (FOPH 2000, RP Acoustics, Leutenbach, Germany) at four focus locations: no steering, x-steering of 5.5 mm, z-steering of +12 mm ($x_F = 0$, $y_F = 0$, $z_F = F + 12$ mm), and z-steering of –12 mm ($x_F = 0$, $y_F = 0$, $z_F = F - 12$ mm). At each focus position, waveforms were acquired within the voltage range from 5 to 50 V in 2-V increments on the Verasonics power supply, corresponding to a range of 39 to 458 V_{pp} at the array element. The resulting dependencies of the focal peak pressures and shock amplitudes on the applied voltage were used to determine BH regimes at different steered focus positions.

G. Ultrasound Imaging

The coaxial US microconvex imaging probe (Vermon CLA7.5, 128 elements, 10 mm radius of curvature, 0.144 mm pitch, elevational focal depth 35 mm, elevational aperture 6 mm) was used for B-mode imaging interleaved with BH pulses. The imaging sequence consisted of 128 ray-lines at 9 MHz center frequency and 60% total bandwidth. Ray-lines were transmitted with a 65 element sub-aperture at a 5 kHz PRF for a 39 Hz framerate and a maximum mechanical index (MI) of 0.33. Each ray-line corresponds to a sector area within the B-mode frame, to which the sector angle was defined in increments of 0.0145 radians or 0.83 degrees. The focusing distance was 50 mm, with a maximum imaging depth of 80 mm. Co-location of the HIFU axial plane and the US imaging plane was confirmed *via* hydrophone scans in water.

The axial position of the HIFU focus z_F = 52 mm corresponded to z_F = 45 mm in the US imaging plane. This position was denoted by a red marker within the B-mode image for targeting and treatment planning.

H. Testing BH Conditions in Polyacrylamide Gel

To confirm the attainment of BH conditions at each of the focus steering locations, sonications in 5% polyacrylamide (PAA) gel phantoms were performed similar to our prior studies [41]. The samples were prepared using a liquid mixture of deionized water and acrylamide/bis-acrylamide 19:1 solution (Fisher Scientific, Bothell, WA, USA) that was degassed for 1 h in a vacuum chamber, poured into a plastic mold with dimensions of 55 × 55 × 70 mm, and polymerized by adding ammonium persulfate and N,N,N′,N′-tetramethyl ethylenediamine (Sigma-Aldrich, St. Louis, MO, USA). The gel was then placed in a custom holder submerged in the tank and attached to the positioning system. The array center of curvature was positioned at a depth of 25 mm in the gel. Electronic steering was applied to place the array focus at the nodes of a rectangular $x_F z_F$ grid, with x_F ranging from –6 to 6 mm with a step of 2 mm, and y_F ranging from 40 to 68 mm with a step of 3 mm.

Each focus position of the steering grid was sonicated with 10-ms long pulses at a 1-Hz PRF with gradually increasing output voltage from 10 to 60 V in 2-V increments. When the voltage reached the threshold necessary to initiate BH, a hyperechoic region appeared at the target site on the coaxial US B-mode image. After the threshold was determined for each focus steering position the “BH steering range” was defined as that corresponding to the threshold voltage increase by 43% relative to the center of curvature. This is equivalent to the 70% pressure amplitude steering contours simulated in the linear regime as described in Section II-C [41].

Finally, a test treatment was performed within the observed BH steering range at the nodes of the aforementioned grid *via* electronic steering. At each treatment node, steering losses were compensated according to the obtained treatment thresholds using the Verasonics apodization feature. This feature smoothly adjusts the effective driving voltage for different steering positions by applying pulse-width modulation during a Verasonics transmit event, controlling the number of “on” and “off” clock cycles [42]. The area outside the steering region was monitored to ensure no grating lobe-related effects appeared outside the region of interest. The volumetric lesion produced was identified using B-mode monitoring and compared to the planned one.

III. RESULTS

A. Optimal Array Parameters

Fig. 4(a) shows a histogram of the allowable z-steering range Δz_F for the generated ensemble of 500 array patterns simulated at an operating frequency of 1.5 MHz. The histogram is divided into 16 intervals of equal length, and the height of each column corresponds to the number of patterns for which the allowable z-steering range Δz_F falls within a given interval. The distribution follows a typical bell-shaped curve, with the steering range Δz_F spanning from 26.2 mm to 27.7 mm. The pattern with the widest steering range $\Delta z_F = 27.7$ mm (Fig. 4(a), arrow) was selected for fabrication and is presented in Fig. 4(b). The equal-area elements of the array (11.7 mm^2) are arranged aperiodically, fully covering the surface except for kerfs with 0.4-mm assumed width.

To select the operating frequency, the simulated pressure amplitude at the array center of curvature, p_F, at 1.5 MHz and 2 MHz were compared, assuming propagation in water and in prostate tissue. In water, the focal gain p_F/p_0 = 30 at 1.5 MHz and p_F/p_0 = 40 at 2 MHz, which matches that of the single-

This article has been accepted for publication in IEEE Transactions on Ultrasonics, Ferroelectrics, and Frequency Control. This is the author's version which has not been fully edited and content may change prior to final publication. Citation information: DOI 10.1109/TUFFC.2025.3596780

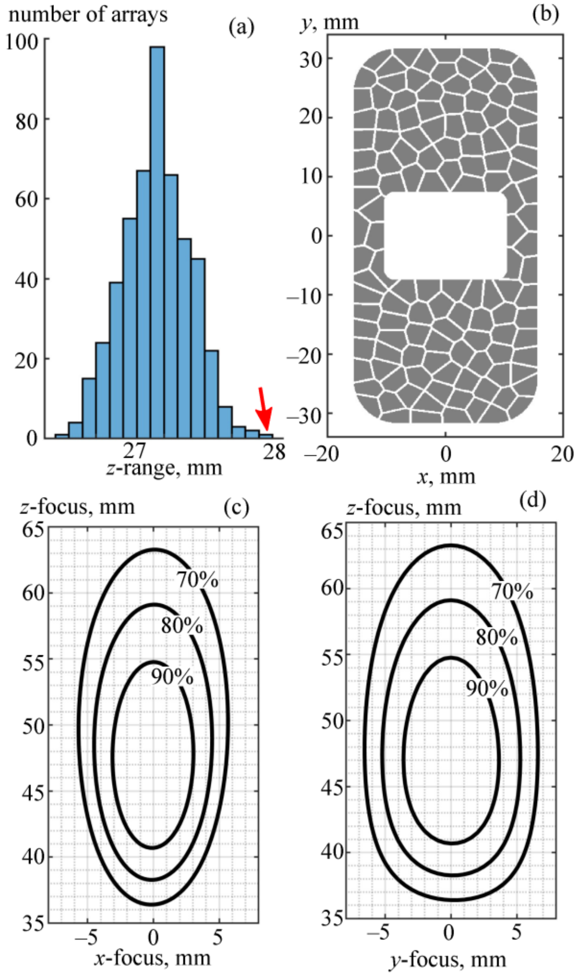

Fig. 4. (a) Histogram of the allowable z-steering range Δz_F for the generated ensemble of 500 arrays. The arrow marks the selected array with the widest steering range. (b) Front-view sketch of the selected array. (c, d) Contours of xz and yz focus steering regions for the selected array. Within these contours, the pressure amplitude at the focus is at least 90%, 80%, and 70% of the maximum achievable value, respectively.

element transrectal BH transducer successfully used previously *in vivo* [19, 20]. Thus, given the same F-number of the strongly focused side, $F_{\#}^{y} = 0.8$, the array was expected to generate a similar nonlinear field in water at comparable intensities at the elements [27, 28].

The *in situ* focal gain in prostate tissue was estimated by multiplying the focal gain in water p_F/p_0 by a scaling coefficient $\exp(-\alpha F)$ that accounts for tissue attenuation: $\alpha = 14.0$ Np/m @ 1.5 MHz, and $\alpha = 18.6$ Np/m @ 2 MHz [43]. The *in situ* focal gains were found to be 14.5 for 1.5 MHz and 15.2 for 2 MHz, therefore, similar initial pressures at the elements would be required to achieve the same focal pressure levels. Given that lower frequencies produce larger BH lesions and result in larger steering range, the frequency of 1.5 MHz was selected as the target operating frequency, with the range of 1.4 – 1.6 MHz. Subsequent simulations of focus steering were performed at the upper end of this range,1.6 MHz, and the results are shown in Fig.4 (c, d) as iso-level contours for relative focal pressure amplitude within $z_F x_F$ and $z_F y_F$ planes. The contours correspond to 90%, 80%, and 70%, of the focal pressure at the center of curvature (i.e. no steering). The amplitude of the grating lobes remained below 30% of the focal amplitude within all contours. Therefore, the contours labeled "70%" outline the allowable focus steering regions (as defined in Section II-C) with dimensions of $\Delta z_F = 27.7$ mm (35.6 mm – 63.3 mm) in the axial direction, $\Delta x_F = 11$ mm (from – 5.5 mm to 5.5 mm) in transverse direction and –6.6 mm to 6.6 mm in elevational direction. Note that the, the $z_F x_F$ range corresponds to the US imaging plane and is thus the most relevant.

B. Breakdown Modes of the Prototype Array

The velocity amplitude and phase distributions at the surface of the 5-element prototype array, back-projected from the hologram, are shown in Fig. 3(c, d). The results are for the 2-MHz single-frequency component of the transient hologram, representing CW case that is representative of a milliseconds-long BH pulse. The pattern of the elements is clearly visible in the reconstructed amplitude distribution in Fig. 3(c). Significant crosstalk was observed between elements 1 and 3, which operated in phase, the kerf between these elements oscillated along with them, making the two separate elements appear indistinguishable. In cases of a phase shift of π (pairs 1 – 2, 2 – 3, and 3 – 4), the kerf exhibited velocity amplitude of zero, as the elements' velocities were always opposite. Finally, in the case of a phase shift of $\pi/2$ (pair 4 – 5), the crosstalk was noticeable, but the elements remained distinguishable: the maximum velocity amplitude inside the kerf was 60% of the maximum amplitude at the surface of the elements.

Despite the noticeable crosstalk, the prototype successfully provided the intended phases at the elements (Fig. 3(c)). The average phase at the surface of elements 1 – 5, expressed as mean ± standard deviation was: $0 \pm 0.06\pi$; $1.07\pi \pm 0.07\pi$; $0.003\pi \pm 0.06\pi$; $1.06\pi \pm 0.07\pi$; and $0.51\pi \pm 0.04\pi$. Given that the intended phases were 0, π, 0, π, $\pi/2$, respectively, all elements fell within the expected range. Notably, heterogeneity in amplitude and phase at the array surface was primarily observed around the solder points of the elements.

Holography-based electroacoustic efficiency calculations showed that the efficiency of the prototype was 83%, which is typical for piezoceramic HIFU arrays [44].

The stress test of the prototype showed that the first breakdown mode is electrical breakdown between opposite-phase elements; specifically, the breakdown between elements 2 and 3 occurred at 650 V_{pp} voltage at the elements (Fig. 3(b)). This output corresponded to 70 V at the Verasonics power supply.

This issue was successfully mitigated by electrically insulating the kerfs with a polymer material: no electrical breakdown was observed at the maximum voltage of 830 V_{pp} at the elements deemed achievable with Verasonics (90 V equivalent). The corresponding acoustic intensity at the surface of the array was 542 W/cm^2, and the characteristic pressure was 4 MPa. The temperature change at the surface of the array remained below 2 °C for the all the voltages tested. Neither conversion efficiency, nor the electrical impedance of the elements changed following the tests, which indicated no lasting mechanical damage.

This article has been accepted for publication in IEEE Transactions on Ultrasonics, Ferroelectrics, and Frequency Control. This is the author's version which has not been fully edited and content may change prior to final publication. Citation information: DOI 10.1109/TUFFC.2025.3596780

C. Fabrication and Characterization of 128-element Array

A photo of the fabricated US-guided endorectal BH probe is shown in Fig. 5(a). The probe included the 128-element HIFU array, with each element connected to the impedance matching network housed in a box with a zif adaptor. Each element was matched to a real impedance of 60 Ohms, with the imaginary part canceled by inductors (see details in Section II-D). The 128-element US imaging probe was integrated within the central opening of the HIFU array and connected through the interconnect to another zif adaptor. The transducer's operating frequency range, based on the highest electroacoustic efficiency (between 65 and 83%), was 1.4–1.6 MHz, and we chose to use the array at 1.6 MHz hereinafter. The array housing included two water ports (Fig 5(b)) to facilitate water circulation within the probe cover, which is mounted on the array for transrectal use.

Both the HIFU array and the US imaging probe were driven by the 256-channel power modified Verasonics Vantage system to produce 1–10 ms BH pulses at a 1% duty cycle, synchronized with US imaging. The Verasonics power supply can provide a driving voltage of up to 80 V peak, resulting in up to 740 V_{pp} at the HIFU-array element. Table I summarizes parameters of the fabricated array described above.

D. Surface Vibrational Velocity Reconstruction

An instantaneous pattern of vibrational velocity back-projected from the transient acoustic hologram to the surface of the BH-array in the case where all elements operated in phase, is shown in Fig. 6(a). It corresponds to the time point $t = 1$ μs, where $t = 0$ corresponds to the beginning of the 3-cycle pulse. Because short pulses do

Fig. 5. (a) Photo of the fabricated BH probe. (b) Zoomed-in view of the BH 128-element array surface with the integrated US imaging probe.

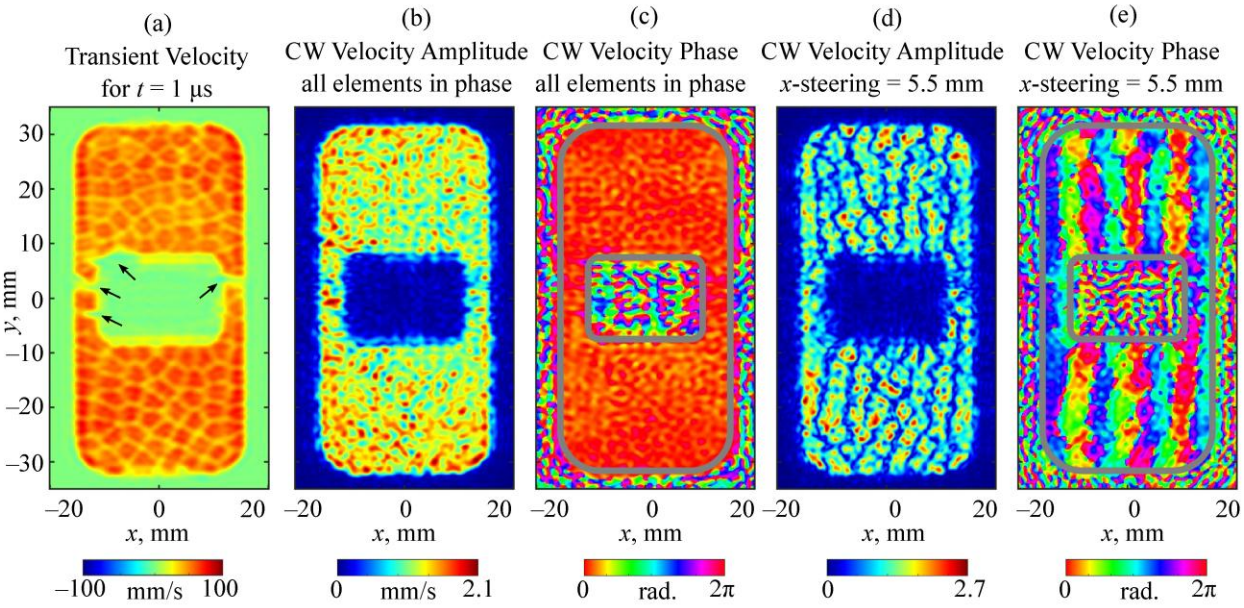

Fig. 6. Back-projection holography results for the BH array. (a) Transient vibrational velocity at the array surface at the time point $t = 1$ μs with all elements operating in phase. Back-projected vibrational velocity amplitude (b) and phase (c) in a CW regime at 1.6 MHz, with all elements operating in phase. CW amplitude (d) and phase (e) distributions for the case of focus steering in the x-direction. The arrows indicate the location of surface defects.

This article has been accepted for publication in IEEE Transactions on Ultrasonics, Ferroelectrics, and Frequency Control. This is the author's version which has not been fully edited and content may change prior to final publication. Citation information: DOI 10.1109/TUFFC.2025.3596780

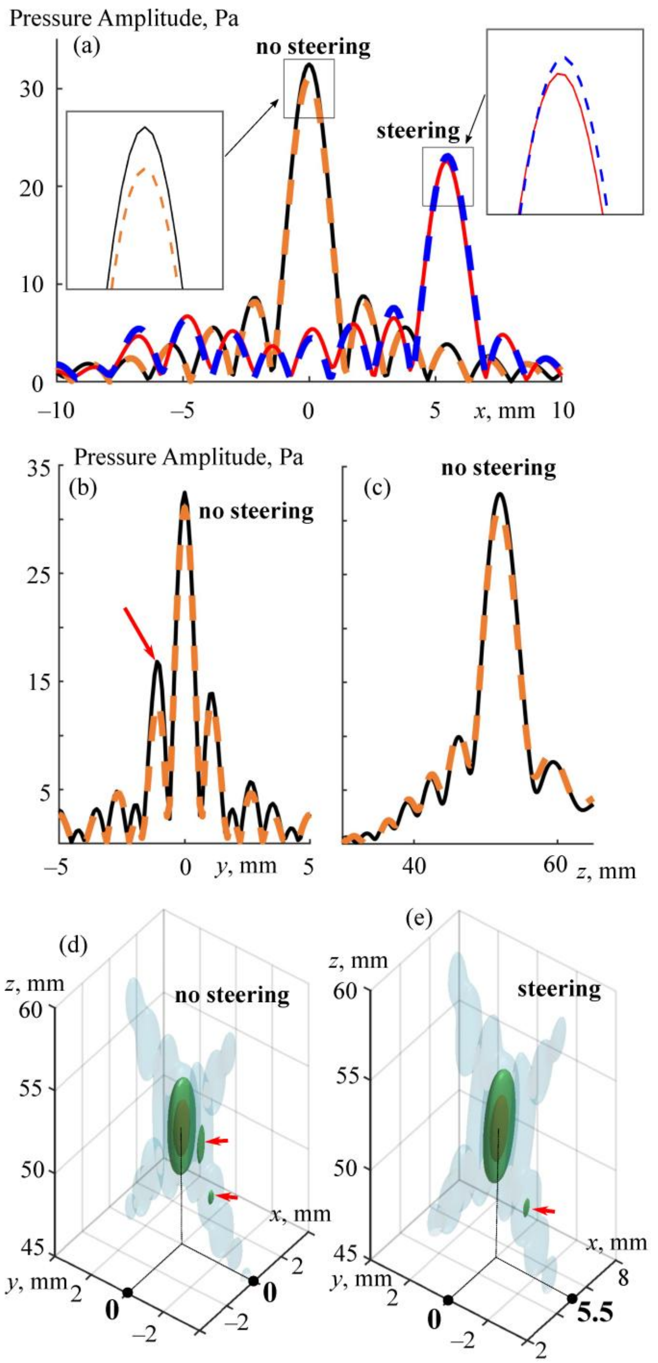

Fig. 7. Pressure amplitude distributions along the *x*-, *y*-, and *z*-directions (a – c) for cases with and without steering. Solid lines represent the real array field forward-projected from the measured hologram, while dashed lines show simulated fields of the idealized array model. (d, e) 3-D field of the real array, presented as iso-surfaces of points with equal pressure amplitude values corresponding to 80%, 50%, and 30% iso-levels of the maximum pressure amplitude. Sidelobes in the focal region are marked with arrows. Bold axis numbers indicate the positions of the non-steered (d) and steered (e) focus.

not generate significant Lamb waves at the surface, small-scale surface defects, element pattern, and functionality can be quickly assessed using this approach [33, 45, 37]. Here, the mosaic distribution of the elements is clearly visible, as are small surface defects around the array opening.

Both the defects and the element pattern are blurred in CW regime at the operating frequency of 1.6 MHz as shown in Fig. 6(b, c) for the vibrational velocity amplitude and phase distributions, respectively. The vibrational velocity pattern demonstrates the oscillation of the entire surface of the array, including the kerfs, making the element pattern indistinguishable. The amplitude distribution was non-uniform due to Lamb waves propagating along the surface of the array in CW regime.

A different oscillation pattern was observed for the case of focus steering ($x_F = 5.5$ mm, $y_F = 0$, $z_F = F$) This steering position corresponds to focusing on the edge of the previously estimated allowable focus steering region (Section III-A). The amplitude within the kerfs between elements (Fig. 6(d)) with significantly different phases (Fig. 6(e)) was close to zero, while elements with similar phases more clearly reveal the presence of crosstalk. As the focus of the array was shifted along the x-axis, the phases at the elements of the array formed vertical lines, which modifying the wavefront shape in the desired direction to focus at the chosen point (x_F, y_F, z_F).

E. Comparison of Measured and Predicted Linear Acoustic Fields of the Array

The linear fields of the fabricated array and the predicted, idealized numerical model of the array were compared to measure the effect of surface imperfections and mechanical crosstalk on the field. The field of the fabricated array at 1.6 MHz was obtained from the hologram (Section II-E), while the idealized field was numerically simulated for the pattern selected for fabrication assuming piston elements with uniform vibration velocity and no crosstalk between them (Section II-C).

Fig. 7(a–c) compare the axial pressure amplitude distributions of the array field along the x-, y-, and z-axes, respectively, for the fabricated (solid lines) and predicted, idealized (dashed lines) array transducers. For the case without focus steering the presence of mechanical crosstalk between the elements, Fig. 7(a–c) ("no steering" labels), is manifested as

TABLE I

SUMMARY OF THE ARRAY PARAMETERS

<table>
<tr><td colspan="6">General parameters</td></tr>
<tr><td colspan="3">Number of elements (N)
128</td><td colspan="3">BH Frequency (f)
1.6 MHz</td></tr>
<tr><td colspan="6">Geometric parameters</td></tr>
<tr><td>$L_x \times L_y$
31×63 mm</td><td>$l_x \times l_y$
21×15 mm</td><td colspan="2">R_{sm}
7 mm</td><td>r_{sm}
2 mm</td><td>h
0.4 mm</td></tr>
<tr><td colspan="6">Allowable steering range in linear regime</td></tr>
<tr><td colspan="2">Δx_F
11 mm</td><td colspan="2">Δy_F
13.2 mm</td><td colspan="2">Δxz_F
27.7 mm</td></tr>
<tr><td colspan="6">Focal lobe size for different steered positions in linear regime ($x \times y \times z$)</td></tr>
<tr><td colspan="2">No Steering/Lateral
1.8×0.8×5.8 mm</td><td colspan="2">Forward
2.1×1.0×8.3 mm</td><td colspan="2">Backward
1.3×0.8×4.0 mm</td></tr>
</table>

$L_x \times L_y$ = aperture size of the array in the x and y directions
$l_x \times l_y$ = opening size of the array in the x and y directions
R_{sm} and r_{sm} = smoothing radii of the outer corners of the array aperture and the opening respectively
h = kerf between the elements
Δx_F, Δy_F, and Δz_F = allowable focus steering range in the x, y, and z directions (linear regime)
Focal lobe size in the linear regime is defined by the 50% amplitude level at various steered focus positions: no steering and the boundaries of the allowable steering range (details in Section III-C).

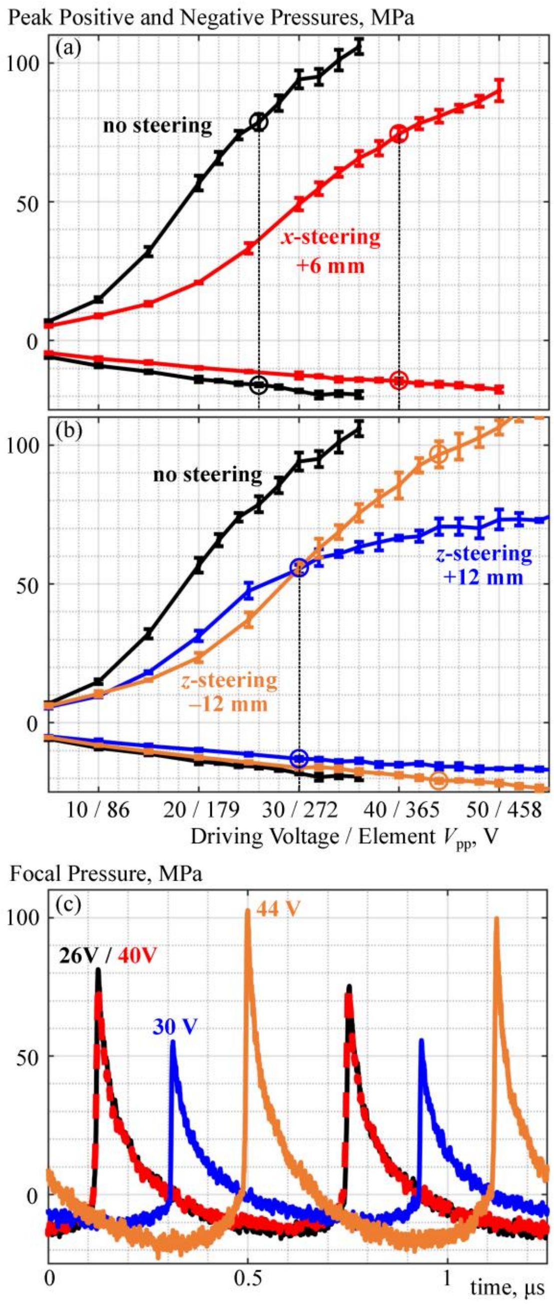

Fig. 8. (a, b) Dependence of the measured peak positive and negative pressures at the focus on the applied Verasonics voltage ("Driving Voltage") for four steered focus positions: no steering, transverse *x*-steering by +6 mm, and axial *z*-steering by +12 mm and –12 mm. Circular markers indicate focal waveforms with fully developed shocks. For reference, the peak-to-peak voltage measured at the array elements is also indicated alongside the Verasonics voltage. (c) Two cycles of measured waveforms with fully developed shocks corresponding to the circular markers. Labels above the waveforms indicate the applied voltages at which the waveforms were measured. A time shift is introduced between the waveforms for visibility.

slightly (by 4.5%) elevated focal pressure compared to the idealized case. This was expected, as the kerfs of the transducer oscillated in phase with the elements (Figs. 6(b)), while they remained completely inactive in the idealized case. Another detail of the fabricated array field is a greater sidelobe level in the elevational y-distribution (Figs. 7(b), arrow), which may be caused by imperfections in the vibrational velocity pattern at the surface of the array.

The pressure distribution for the case with transverse focus steering ($x_F = 5.5$ mm, $y_F = 0$, $z_F = F$) is presented in Fig. 7(a) ("steering" label). It demonstrates the opposite effect of destructive crosstalk, which disturbed the independently set steering phases at the elements. As a result, the maximum pressure amplitude for the fabricated transducer was 2.4% lower than that of the idealized one. The focal pressure of the fabricated transducer in the steered case was 69% of that without steering, confirming the theoretically predicted 70%-edge of the allowable focus steering region. Thus, the results show that even though crosstalk and Lamb waves existed on the surface of the array, their effect did not significantly change the field pattern and did not change the focal pressure by more than 4.5% compared to the idealized case.

A more comprehensive 3-D representation of the field of the fabricated transducer for the cases without and with steering is provided in Figs. 7(d–e). The fields are presented as iso-surfaces of pressure amplitude corresponding to three levels: 80%, 50%, and 30%, of the maximum pressure amplitude. Two 50%-level sidelobes were observed in the 30%-level focal region (Fig. 7(d), arrow markers), while the focus steering resulted in the suppression of one of the lobes (Fig. 7(d), arrow marker). No grating lobes greater than 30% of the pressure amplitude appeared outside the focal region.

Figs. 7(d) and (e) show the main focal lobe delineated by the 50% pressure amplitude level (50%-level isosurfaces). The focal lobe size remains unchanged when the focus is steered in the x-direction (Fig. 7(e)) compared to the unsteered case (Fig. 7(d)). In both cases, the lobe dimensions along the x, y, and z axes are 1.8×0.8×5.8 mm. Note that in the steered case (Fig. 7(e)), the lobe is rotated relative to the coordinate axes of the transducer. Thus, the dimensions were measured along the x, y, and z axes but aligned with the lobe's symmetry axes. The same lobe size (1.8×0.8×5.8 mm) was observed for y-steering ($x_F = 0$, $y_F = \pm 6.6$ mm, $z_F = F$). However, substantial differences were seen for z-steering. When steering away from the transducer ($x_F = 0$, $y_F = 0$, $z_F = 63.3$ mm) the lobe enlarged to 2.1×1.0×8.3 mm, while steering towards the transducer ($x_F = 0$, $y_F = 0$, $z_F = 35.6$ mm) reduced the lobe to 1.3×0.8×4.0 mm.

F. Nonlinear Field Measurements

Figs. 8(a–b) present the dependence of peak positive and peak negative focal pressures on system driving voltage for four focus positions. These positions were selected near the z and x steering limits of the "70%" theoretically predicted steering range (Fig. 4(c)) in the linear regime. Fig. 8(a) compares the curves for the case without steering, and the transverse x-steering at the position $x_F = 6$ mm, while Fig. 8(b) provides the same comparison between the case with no steering and two cases of z-steering to $x_F = 12$ mm and – 12 mm. In all cases, peak pressures increased with the system driving voltage, with typical saturation behavior at higher outputs due to nonlinear propagation effects and shock formation [27]. Circular markers in Figs. 8(a–b) indicate the points corresponding to focal waveforms with a fully

This article has been accepted for publication in IEEE Transactions on Ultrasonics, Ferroelectrics, and Frequency Control. This is the author's version which has not been fully edited and content may change prior to final publication. Citation information: DOI 10.1109/TUFFC.2025.3596780

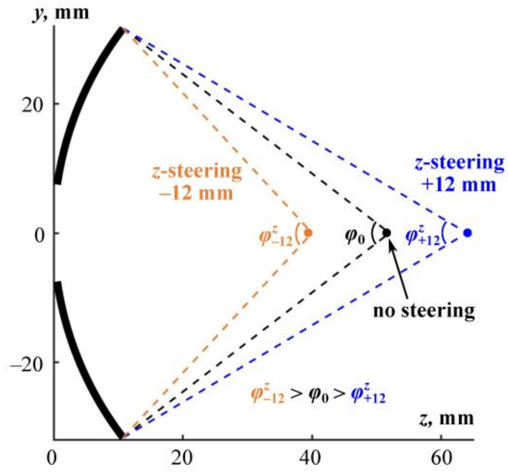

Fig. 9. Sketch, illustrating changes in the focusing angle φ^z when steering the focus along the *z*-axis by –12 mm (φ^z_{-12}) and +12 mm (φ^z_{+12}).

developed shock, defined as the shock front with the lower boundary corresponding to zero pressure, i.e. shock amplitude being equal to peak positive pressure [27]. Two cycles of the corresponding focal pressure waveforms are shown in Fig. 8(c). The waveforms corresponding to no-steering and *x*-steering cases were obtained at the driving voltages of 26 V and 40 V, respectively. As expected, because the focusing angle (or the *F*-number) did not change appreciably with transverse steering, the waveforms were nearly identical, with peak positive pressures of 79 MPa and 74 MPa, and peak negative pressures of 15.8 MPa and 14.5 MPa for no-steering and steered cases, respectively [41].

In the case of steering along *z*-axis, as illustrated in Fig. 9, the focusing angle changed substantially when steering within the allowable range of ±12 mm identified in the linear regime. Accordingly, the developed shock formed at a higher system driving voltage and corresponded to higher peak focal pressures (p_+ = 97 ± 5 MPa and p_- = –20.9 ± 0.8 MPa at a voltage of 44 V) when steering closer to the transducer than further away from it (p_+ = 55 ± 2 MPa and p_- = –13.0 ± 0.7 MPa at a driving voltage of 30 V).

A notable detail is that strongly nonlinear focal waveforms measured with the FOPH hydrophone – particularly in cases of high-frequency and highly focused transducers – underestimate peak positive pressures. This underestimation arises due to the finite sampling rate of the output data and the tight transverse size of the strongly nonlinear focal lobe, which is smaller than the 100-µm active area of the hydrophone. In the present case of a 1.6-MHz frequency and an *F*-number $F_{\#}^{y}$ = 0.8 for the strongly focused side, the expected peak positive pressure underestimation error is approximately 15–20% [46, 41].

G. BH Exposures of Tissue-Mimicking Gel Phantoms

An example of a B-mode image obtained at a target point with coordinates x_F = –2 mm, y_F = 0 mm, z_F = 64 mm after a single BH pulse delivered to the PAA gel is shown in Fig. 10(a). The size of a hyperechoic region was 1.5 mm in the radial direction and 2 mm in the axial direction. The distribution of the threshold voltage values sufficient to reach BH conditions ("BH Voltage") for all focus positions within focus steering range is shown in Fig. 10(b). The contour presented in the figure represents the BH steering range, equivalent to the "70%" theoretically predicted steering range in the linear regime (Fig. 4(c)). Given that the minimum BH Voltage of 26 V was observed at the center of curvature, the corresponding compensated voltage equivalent to the 70% range was 26/0.7 = 37.1 V. The contour in Fig. 10(b) represents the isoline of this compensated voltage of 37.1 V.

The shape of the contours was similar to the one obtained from linear simulations (Fig. 4(c), "70%"), but there were some differences due to nonlinear effects. The BH steering range in the axial direction within the 37.1-V contour obtained in the BH experiment (Fig. 10(b), solid contour) spanned from 40 mm to 65.5 mm, whereas in the case of the 70% pressure amplitude contour obtained *via* simulations, the range was from 35.6 mm to 63.3 mm (Fig. 4(c)).

The explanation for this difference is again based on the focusing angle: even though the developed shocks required for BH have lower peak pressures for smaller focusing angles, a lower driving voltage is required to achieve them [27]. This effect enlarged the *z*-steering range in the positive direction as the focusing angle decreased with steering ($\varphi^z_{+12} < \varphi_0$, Fig. 9): the upper *z*-limit of the BH steering range was 65.5 mm compared to 63.3 mm in the linear case. *z*-steering in the negative direction led to an increase in the focusing angle ($\varphi^z_{-12} > \varphi_0$, Fig. 9) and a decrease in the steering range – the lower *z*-limit was 40 mm *vs.* 35.6 mm for the BH and theoretical regions, respectively.

Radial steering in the x-direction did not significantly change the focusing angle. Thus, the ranges of ±5.5 mm for the theoretical region and ±6 mm for the BH region were comparable.

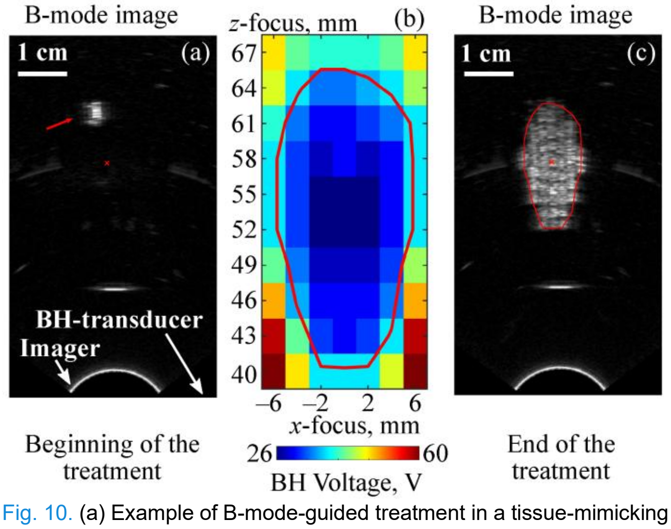

Fig. 10. (a) Example of B-mode-guided treatment in a tissue-mimicking PAA gel phantom. The arrow marks hyperechoic regions corresponding to the current positions of the focus during treatment. (b) 2-D map of threshold voltage values required to induce BH exposure for different steered focus positions. The contour represents the "BH steering range", where the threshold voltage does not exceed 37 V. (c) Treatment results within the BH steering contour, visualized *via* B-mode guidance. The hyperechoic area shows residual BH bubbles after treatment. "Cross" markers in (a) and (c) indicate the position of the center of curvature of the array.

Fig.10(c) shows an example of a B-mode image after a BH treatment throughout the focus steering range performed with automated driving voltage compensation *via* apodization (Section II-H) according to the threshold measured for each point, as described above. All of the treated points appeared hyperechoic, indicating the attainment of BH exposure conditions. They completely covered the planned steering region (solid contour) and produced a lesion with the 25.5 × 12 mm dimensions. No evidence of bubble activity was detected outside the region of interest during or after the treatment, confirming the absence of grating lobes that could compromise the safety of the procedure.

IV. DISCUSSION AND CONCLUSION

This paper presents a novel design for an US image-guided 128-element array for transrectal BH mechanical ablation of the prostate and demonstrates the feasibility thereof. The randomized, fully populated pattern of elements enables 3-D electronic focus steering while maintaining a low level of grating lobes. Although the most practical steering directions are within the US imaging plane xz (Fig. 1(b)), so the bubble activity can be monitored in real time during treatment, the array is also capable of steering along the elevational direction. This capability can be useful for BH procedures with pre-treatment planning, where 3-D ablation is possible without real-time guidance. An important practical consideration is that the allowable focus steering region, with a characteristic size of 26 mm axially and 12 mm laterally, is not intended to be used without mechanical repositioning of the transducer. The transducer will still be shifted in the y-direction and rotated around the y-axis to ablate larger targets, but the number of repositioning events will be minimized. Additionally, the probe cover filled with liquid for acoustic coupling between the transducer and the rectal wall (Fig. 1(a)) – can be inflated or deflated to adjust the target position in the z-direction. The x-steering capability is particularly critical, as the alternative mechanical method – rotating the probe – often leads to gas bubble entrapment between the probe cover and the rectal wall. In some cases, this can only be resolved by removing the probe from the rectum and reapplying coupling gel, which is time-consuming and increases the overall procedure time. The y-steering capability of the array was not tested in this study because in this case treatment progression cannot be visualized in real time using the central imaging probe. However, y-steering could still be useful for other purposes, for example to facilitate volumetric HIFU-push shear wave elastography (SWE) mapping prior to treatment [47].

An advantage of the developed system is that both the HIFU and the US imaging arrays are driven by a single Verasonics Vantage system, which minimizes the system footprint and allows seamless synchronization of BH pulses with US imaging.

The goal of this study was to develop an array with BH capabilities; however, the fully populated design may also benefit various other HIFU applications. The dense element packing can reduce the overall device size. Further, the low level of grating lobes is even more critical for thermal HIFU applications than for BH, as it prevents unwanted heating outside the treatment region. Additionally, the 2-D array pattern can be utilized for aberration correction in various scenarios [27, 28, 48, 49, 50].

The final fully populated array design was selected based on an ensemble of 500 randomly generated array patterns. The selection was based on maximizing the focus steering range Δz_F in the axial direction, which was identified as the most critical parameter for practical use. However, because Δz_F primarily depends on the array curvature and the size of the elements, its standard deviation was quite small, and a smaller ensemble of patterns would most likely have been sufficient. Thus, the choice of the ensemble size in designing the fully populated pattern is generally dictated by the performance parameter being optimized. For example, it would be larger to minimize the level of grating lobes [25].

An important finding of this study is that fully populated arrays made from PZT-4 ceramic perform well in terms of electronic focus steering despite crosstalk between elements. While holography-based reconstruction of the fabricated array's surface vibrations revealed noticeable crosstalk when the focus was steered, this resulted in only a 2.4% decrease in focal pressure amplitude compared to an idealized model with no crosstalk (see Section III-E). Therefore, fully populated arrays made of PZT may serve as a viable alternative to piezocomposite arrays, which exhibit less crosstalk but have so far been considered more fragile and prone to heat-induced damage [26]. Importantly, the presented PZT design demonstrates safe operation at an extremely high initial intensity at the elements – up to 542 W/cm^2 (corresponding to initial pressure at the elements of 4 MPa) – which significantly exceeds the limit of 30 W/cm^2 commonly reported by manufacturers [41]. As the presented fully populated BH array made of PZT was fabricated recently, and is the first of its kind, its durability over time is not immediately known and will be evaluated in the future. We do not expect the mechanical crosstalk between elements to pose a durability issue since surface waves are typical in PZT HIFU transducers and do not usually cause damage.

Measurements of the array's nonlinear field demonstrated that it could generate nonlinear waveforms with peak pressures and shock amplitudes sufficient to initiate BH mechanisms.

Theoretical simulations of the allowable focus steering range, performed within the linear model (Section III-A), provided a reasonable estimate of the experimentally obtained BH steering range in the nonlinear case (Section III-G). In the case considered, the difference in steering ranges between the linear and nonlinear cases was 1 mm in the transverse x-direction and 2.1 mm in the axial z-direction. Due to the dependence of nonlinear propagation effects on the transducer's focusing angle, the lower and upper z-boundaries of the nonlinear steering range were shifted by +4.3 mm and +2.2 mm, respectively, compared to the linear steering range. This finding, previously reported in [41], significantly simplifies the transducer design process, as fast linear simulations can be used to estimate steering performance for multiple array variants, whereas nonlinear simulations of focus steering are significantly more time-consuming [51].

Changes in the focusing angle during steering explain the differences in focal lobe size observed between steered and unsteered cases. Because larger focusing angles lead to smaller

This article has been accepted for publication in IEEE Transactions on Ultrasonics, Ferroelectrics, and Frequency Control. This is the author's version which has not been fully edited and content may change prior to final publication. Citation information: DOI 10.1109/TUFFC.2025.3596780

focal lobe sizes [27], z-steering away from the transducer increases the lobe size, while z-steering towards the transducer reduces it, as confirmed by linear simulations. In contrast, x- and y-steering do not significantly affect the lobe size, as they induce only minimal changes in the focusing angle.

A successful test of the array performance in volumetric ablation was conducted using optically transparent PAA gel. This approach represents an important step toward using the array in real tissues. Translation of these results to prostate can be achieved using a derating procedure [52, 11]. According to this method, shock amplitude and peak pressures in tissue will match those in the lossless gel if a higher driving voltage is applied to compensate for linear energy losses in the prefocal region. The compensation coefficient $\exp(\alpha\Delta l)$ is based on the attenuation α and the focusing depth Δl in tissue. Thus, driving voltage requirements for the prostate can be predicted for specific treatment cases given the known attenuation α at the driving frequency. For example, in an *in vivo* BH study using a single-element transrectal BH array in a canine model, a 60% increase in voltage was required compared to PAA gel [19, 20]. This indicates that the fabricated array has a significant power reserve. In the PAA gel, within the “BH steering range”, the threshold voltage did not exceed 37 V (Fig. 10(b)), thus, given that the system’s voltage limit is 80 V, an additional increase of over 115% is available.

Future testing of the fabricated array will confirm its performance in *ex vivo* human prostate tissues to prepare for pre-clinical *in vivo* experiments in canine model. The results of the testing will be used to apply for investigational device exemption (IDE) Food and Drug Administration (FDA) approval to proceed with clinical studies.

Finally, it is important to note that the proposed array design algorithm is not limited to transrectal BH arrays but can be applied to various HIFU transducer designs.

ACKNOWLEDGMENT

The authors would like to thank Pamela Hamilton for creating the illustration in Fig. 1(a) and Bryan Cunitz for designing the power-enhanced HIFU version of Verasonics Vantage used in this work to achieve BH regime.

P.B. Rosnitskiy and T.D. Khokhlova are with the Department of Medicine, Division of Gastroenterology, University of Washington, Seattle, WA 98104 USA (e-mail: pavrosni@gmail.com).

G.P.L. Thomas is with the Applied Physics Laboratory, University of Washington, Seattle, WA 98105 USA.

G.L. Lee is with the Department of Bioengineering, University of Washington, Seattle, WA 98105 USA.

V.A. Khokhlova and O.A. Sapozhnikov are with the Applied Physics Laboratory, University of Washington, Seattle, WA 98105 USA, and also with M. V. Lomonosov Moscow State University, 119991 Moscow, Russia.

G.R. Schade is with the Department of Urology, University of Washington, Seattle, WA 98195 USA.

K.P. Morrison and F. Chavez are with Sonic Concepts, Inc., Bothell, WA 98011 USA.

REFERENCES

[1] E. R. Cordeiro, X. Cathelineau, S. Thüroff, M. Marberger, S. Crouzet, and J. J. M. C. H. de la Rosette, “High-intensity focused ultrasound (HIFU) for definitive treatment of prostate cancer,” *BJU International*, vol. 110, no. 9. Wiley, pp. 1228–1242, 06-Jun-2012.

[2] S. Guillaumier, *et al.*, “A Multicentre Study of 5-year Outcomes Following Focal Therapy in Treating Clinically Significant Nonmetastatic Prostate Cancer,” *European Urology*, vol. 74, no. 4. Elsevier BV, pp. 422–429, Oct-2018.

[3] M. J. Johnston, A. Emara, M. Noureldin, S. Bott, and R. G. Hindley, “Focal High-intensity Focussed Ultrasound Partial Gland Ablation for the Treatment of Localised Prostate Cancer: A Report of Medium-term Outcomes From a Single-center in the United Kingdom,” *Urology*, vol. 133. Elsevier BV, pp. 175–181, Nov-2019.

[4] L. R. Abrams, M. O. Koch, and C. D. Bahler, “Focal High-Intensity Focused Ultrasound Ablation of the Prostate,” *Journal of Endourology*, vol. 35, no. S2. Mary Ann Liebert Inc, p. S-24-S-32, 01-Sep-2021.

[5] M. Dellabella, A. Branchi, M. Di Rosa, M. Pucci, L. Gasparri, R. Claudini, F. Carnevali, S. Cecchini, and D. Castellani, “Oncological and functional outcome after partial prostate HIFU ablation with Focal-One®: a prospective single-center study,” *Prostate Cancer and Prostatic Diseases*, vol. 24, no. 4. Springer Science and Business Media LLC, pp. 1189–1197, 18-May-2021.

[6] Focal One® HIFU Technology. [Online]. Accessed: May 5, 2025, Available https://focalone.com/hifu-technology/

[7] M. I. Skolnik, *Introduction to Radar Systems*. New York, NY, USA: McGraw-Hill, 1962.

[8] P. M. Gschwend, J. M. Hintze, I. K. Herrmann, S. E. Pratsinis, and F. H. L. Starsich, “Precision in Thermal Therapy: Clinical Requirements and Solutions from Nanotechnology,” *Advanced Therapeutics*, vol. 4, no. 2. Wiley, 27-Jan-2021.

[9] A. M. Lake, T. L. Hall, K. Kieran, J. B. Fowlkes, C. A. Cain, and W. W. Roberts, “Histotripsy: Minimally Invasive Technology for Prostatic Tissue Ablation in an *In Vivo* Canine Model,” *Urology*, vol. 72, no. 3. Elsevier BV, pp. 682–686, Sep-2008.

[10] J. E. Parsons, C. A. Cain, G. D. Abrams, and J. B. Fowlkes, “Pulsed cavitational ultrasound therapy for controlled tissue homogenization,” *Ultrasound in Medicine and Biology*, vol. 32, no. 1. Elsevier BV, pp. 115–129, Jan-2006.

[11] T. D. Khokhlova, M. S. Canney, V. A. Khokhlova, O. A. Sapozhnikov, L. A. Crum, and M. R. Bailey, “Controlled tissue emulsification produced by high intensity focused ultrasound shock waves and millisecond boiling,” *The Journal of the Acoustical Society of America*, vol. 130, no. 5. Acoustical Society of America (ASA), pp. 3498–3510, 01-Nov-2011.

[12] R. P. Williams, J. C. Simon, V. A. Khokhlova, O. A. Sapozhnikov, and T. D. Khokhlova, “The histotripsy spectrum: differences and similarities in techniques and instrumentation,” *International Journal of Hyperthermia*, vol. 40, no. 1. Informa UK Limited, 17-Jul-2023.

[13] V. A. Khokhlova, J. B. Fowlkes, W. W. Roberts, G. R. Schade, Z. Xu, T. D. Khokhlova, T. L. Hall, A. D. Maxwell, Y.-N. Wang, and C. A. Cain, “Histotripsy methods in mechanical disintegration of tissue: Towards clinical applications,” *International Journal of Hyperthermia*, vol. 31, no. 2. Informa UK Limited, pp. 145–162, 17-Feb-2015.

[14] G. R. Schade, T. L. Hall, and W. W. Roberts, “Urethral-sparing Histotripsy of the Prostate in a Canine Model,” *Urology*, vol. 80, no. 3. Elsevier BV, pp. 730–735, Sep-2012.

[15] G. R. Schade, J. Keller, K. Ives, X. Cheng, T. J. Rosol, E. Keller, and W. W. Roberts, “Histotripsy Focal Ablation of Implanted Prostate Tumor in an ACE-1 Canine Cancer Model,” *Journal of Urology*, vol. 188, no. 5. Ovid Technologies (Wolters Kluwer Health), pp. 1957–1964, Nov-2012.

[16] T. G. Schuster, J. T. Wei, K. Hendlin, R. Jahnke, and W. W. Roberts, “Histotripsy Treatment of Benign Prostatic Enlargement Using the Vortx R_x System: Initial Human Safety and Efficacy Outcomes,” *Urology*, vol. 114. Elsevier BV, pp. 184–187, Apr-2018.

[17] V.A. Khokhlova, P.B. Rosnitskiy, S.A. Tsysar, S.V. Buravkov, O.A. Sapozhnikov, M. M. Karzova, T.D. Khokhlova, A.D. Maxwell, N.M. Gaifullin, A.V. Kadrev, D. A. Okhobotov, A.A. Kamalov, G.R. Schade, “A novel method for non-invasive mechanical ablation of prostate tumors using pulsed focused ultrasound,” *Urologiia,* vol. 6, pp. 67–73, 2019.

[18] V.A. Khokhlova, “Boiling histotripsy for focal therapy in prostate,” presented at the 12th *International Symposium on Focal Therapy and Imaging in Prostate and Kidney Cancer*, Washington, DC, USA, Feb 9 – 11, 2020.

This article has been accepted for publication in IEEE Transactions on Ultrasonics, Ferroelectrics, and Frequency Control. This is the author's version which has not been fully edited and content may change prior to final publication. Citation information: DOI 10.1109/TUFFC.2025.3596780

[19] G.R. Schade, T.D. Khokhlova, C. Hunter, W. Kreider, P.B. Rosnitskiy, P.V. Yuldashev, O.A. Sapozhnikov, V.A. Khokhlova. “A preclinical transrectal boiling histotripsy system for prostate ablation,” in *Abstract Book of the 34rd Annual Meeting of Engineering and Urology Society (EUS)*, Chicago, IL, USA, 2019, pp. 46.

[20] G. Schade, R. Sekar, T. Khokhlova, A. Peek, Y.-N. Wang, S. Totten, W. Kreider, Y. Kumar, O. Sapozhnikov, A. Maxwell, V. Khokhlova. “Transrectal boiling histotripsy of the prostate: initial pre-clinical results with a prototype device,” presented at the *7th International Symposium on Focused Ultrasound*, Online, Nov 9 – 13, 2020.

[21] V. A. Khokhlova, P. B. Rosnitskiy, S. A. Tsysar, S. V. Buravkov, E. M. Ponomarchuk, O. A. Sapozhnikov, M. M. Karzova, T. D. Khokhlova, A. D. Maxwell, Y.-N. Wang, A. V. Kadrev, A. L. Chernyaev, V. P. Chernikov, D. A. Okhobotov, A. A. Kamalov, and G. R. Schade, “Initial Assessment of Boiling Histotripsy for Mechanical Ablation of *Ex Vivo* Human Prostate Tissue,” *Ultrasound in Medicine and Biology*, vol. 49, no. 1. Elsevier BV, pp. 62–71, Jan-2023.

[22] P. B. Rosnitskiy, S. A. Tsysar, M. M. Karzova, S. V. Buravkov, P. G. Malkov, N. V. Danilova, E. M. Ponomarchuk, O. A. Sapozhnikov, T. D. Khokhlova, G. R. Schade, A. D. Maxwell, Y.-N. Wang, A. V. Kadrev, A. L. Chernyaev, D. A. Okhobotov, A. A. Kamalov, and V. A. Khokhlova, “Pilot *ex vivo* study on non-thermal ablation of human prostate adenocarcinoma tissue using boiling histotripsy,” *Ultrasonics*, vol. 133. Elsevier BV, p. 107029, Aug-2023

[23] Y. N. Kumar, Z. Singh, Y.-N. Wang, D. Kanabolo, L. Chen, M. Bruce, E. Vlaisavljevich, L. True, A. D. Maxwell, and G. R. Schade, “A comparative study of histotripsy parameters for the treatment of fibrotic *ex-vivo* human benign prostatic hyperplasia tissue,” *Scientific Reports*, vol. 14, no. 1. Springer Science and Business Media LLC, 02-Sep-2024.

[24] P. B. Rosnitskiy, B. A. Vysokanov, L. R. Gavrilov, O. A. Sapozhnikov and V. A. Khokhlova, "Method for Designing Multielement Fully Populated Random Phased Arrays for Ultrasound Surgery Applications," *IEEE Transactions on Ultrasonics, Ferroelectrics, and Frequency Control*, vol. 65, no. 4, pp. 630-637, April 2018

[25] P. B. Rosnitskiy, O. A. Sapozhnikov, L. R. Gavrilov, and V. A. Khokhlova, “Designing Fully Populated Phased Arrays for Noninvasive Ultrasound Surgery with Controlled Degree of Irregularity in the Arrangement of Elements,” *Acoustical Physics*, vol. 66, no. 4. Pleiades Publishing Ltd, pp. 352–361, Jul-2020.

[26] S. A. Tsysar, P. B. Rosnitskiy, S. A. Asfandiyarov, S. A. Petrosyan, V. A. Khokhlova, and O. A. Sapozhnikov, “Phase Correction of the Channels of a Fully Populated Randomized Multielement Therapeutic Array Using the Acoustic Holography Method,” *Acoustical Physics*, vol. 70, no. 1. Pleiades Publishing Ltd, pp. 82–89, Feb. 2024.

[27] P. B. Rosnitskiy *et al.*, “Design of HIFU transducers for generating specified nonlinear ultrasound fields,” *IEEE Trans. Ultrason., Ferroelectr., Freq. Control*, vol. 64, no. 2, pp. 374–390, Feb. 2017.

[28] M. M. Karzova, P. V. Yuldashev, V. A. Khokhlova, F. A. Nartov, K. P. Morrison, and T. D. Khokhlova, “Dual-Use Transducer for Ultrasound Imaging and Pulsed Focused Ultrasound Therapy,” *IEEE Transactions on Ultrasonics, Ferroelectrics, and Frequency Control*, vol. 68, no. 9. Institute of Electrical and Electronics Engineers (IEEE), pp. 2930–2941, Sep-2021.

[29]V.A. Khokhlova, P.B. Rosnitskiy, P.V. Yuldashev, T.D. Khokhlova, O.A. Sapozhnikov, L.R. Gavrilov, M.M. Karzova, G. R. Schade, “Design of a transrectal probe for boiling histotripsy ablation of prostate,” in *Final Program and Abstract Book of the 18th International Symposium on Therapeutic Ultrasound*, Nashville, TN, USA, 2018, pp. 67 – 69.

[30] V.A. Khokhlova *et al.*, “Boiling histotripsy ablation of *ex vivo* human prostate tissues with benign hyperplasia and adenocarcinoma,” presented at the *22nd Annual International Symposium for Therapeutic Ultrasound/6th European Symposium of EUFUS*, Lyon, France, April 17 – 20, 2023.

[31] T. D. Khokhlova, Y. A. Haider, A. D. Maxwell, W. Kreider, M. R. Bailey, and V. A. Khokhlova, “Dependence of Boiling Histotripsy Treatment Efficiency on HIFU Frequency and Focal Pressure Levels,” *Ultrasound in Medicine and Biology*, vol. 43, no. 9. Elsevier BV, pp. 1975–1985, Sep-2017.

[32] M. Balzer, T. Schlömer, and O. Deussen, “Capacity-constrained point distributions: A variant of Lloyd’s method,” *ACM Trans. Graph.*, vol. 28, no. 3, pp. 1–8, 2009.

[33] P. B. Rosnitskiy *et al.*, "xDDx: A Numerical Toolbox for Ultrasound Transducer Characterization and Design With Acoustic Holography," in *IEEE Transactions on Ultrasonics, Ferroelectrics, and Frequency Control*, vol. 72, no. 5, pp. 564–580, 2025.

[34] L. R. Gavrilov, O. A. Sapozhnikov, and V. A. Khokhlova, “Spiral arrangement of elements of two-dimensional ultrasonic therapeutic arrays as a way of increasing the intensity at the focus,” *Bull. Russian Acad. Sci.*, Phys., vol. 79, no. 10, pp. 1232–1237, 2015.

[35] S. A. Ilyin, P. V. Yuldashev, V. A. Khokhlova, L. R. Gavrilov, P. B. Rosnitskiy, and O. A. Sapozhnikov, “Analytical method for evaluating the quality of acoustic fields radiated by a multielement therapeutic array with electronic focus steering,” *Acoust. Phys.*, vol. 61, no. 1, pp. 52–59, 2015.

[36] A. D. Maxwell *et al.,* “A Prototype Therapy System for Transcutaneous Application of Boiling Histotripsy,” *IEEE Trans. Ultrason., Ferroelect., Freq. Control*, vol. 64, no. 10, pp. 1542–1557, Oct. 2017.

[37] O. A. Sapozhnikov, S. A. Tsysar, V. A. Khokhlova, and W. Kreider, “Acoustic holography as a metrological tool for characterizing medical ultrasound sources and fields,” *The Journal of the Acoustical Society of America*, vol. 138, no. 3. Acoustical Society of America (ASA), pp. 1515–1532, Sep. 01, 2015.

[38] R. P. Williams, W. Kreider, F. A. Nartov, M. M. Karzova, V. A. Khokhlova, O. A. Sapozhnikov, and T. D. Khokhlova, “Synthesized acoustic holography: A method to evaluate steering and focusing performance of ultrasound arrays,” *The Journal of the Acoustical Society of America*, vol. 157, no. 4. Acoustical Society of America (ASA), pp. 2750–2762, 01-Apr-2025.

[39] P. B. Rosnitskiy, O. A. Sapozhnikov, V. A. Khokhlova, W. Kreider, T. D. Khokhlova, xDDx: User Manual Accessed: Feb. 11, 2025. [Online]. Available: https://github.com/pavrosni/xDDx/releases

[40] O. A. Sapozhnikov and M. R. Bailey, “Radiation force of an arbitrary acoustic beam on an elastic sphere in a fluid,” *The Journal of the Acoustical Society of America*, vol. 133, no. 2. Acoustical Society of America (ASA), pp. 661–676, Jan. 30, 2013.

[41] C. R. Bawiec *et al.*, “A prototype therapy system for boiling histotripsy in abdominal targets based on a 256-element spiral array,” *IEEE Trans. Ultrason., Ferroelectr., Freq. Control*, vol. 68, no. 5, pp. 1496–1510, May 2021.

[42] M. A. Ghanem, A. D. Maxwell, W. Kreider, B. W. Cunitz, V. A. Khokhlova, O. A. Sapozhnikov, and M. R. Bailey, “Field Characterization and Compensation of Vibrational Nonuniformity for a 256-Element Focused Ultrasound Phased Array,” *IEEE Transactions on Ultrasonics, Ferroelectrics, and Frequency Control*, vol. 65, no. 9. Institute of Electrical and Electronics Engineers (IEEE), pp. 1618–1630, Sep-2018.

[43]P. A. Hasgall *et al.* (Feb. 22, 2022). IT’IS Database for Thermal and Electromagnetic Parameters of Biological Tissues, Version 4.1. [Online]. Accessed: May 5, 2025, Available: https://itis.swiss/virtual-population/tissueproperties/database/acoustic-properties/

[44] SonicConcepts HIFUPlex™ Portfolio. [Online]. Accessed: May 5, 2025, Available: https://sonicconcepts.com/hifuplex/

[45] D. Cathignol, O. A. Sapozhnikov, and J. Zhang, “Lamb waves in piezoelectric focused radiator as a reason for discrepancy between O’Neil’s formula and experiment,” *The Journal of the Acoustical Society of America*, vol. 101, no. 3. Acoustical Society of America (ASA), pp. 1286–1297, Mar. 01, 1997.

[46] C. R. Bawiec, P. B. Rosnitskiy, A. T. Peek, A. D. Maxwell, W. Kreider, G. R. ter Haar, O. A. Sapozhnikov, V. A. Khokhlova, and T. D. Khokhlova, “Inertial Cavitation Behaviors Induced by Nonlinear Focused Ultrasound Pulses,” *IEEE Transactions on Ultrasonics, Ferroelectrics, and Frequency Control*, vol. 68, no. 9. Institute of Electrical and Electronics Engineers (IEEE), pp. 2884–2895, Sep-2021.

[47] G.L. Lee, O.A. Sapozhnikov, M. Song, G. Thomas, P. Rosnitskiy, G.R. Schade, T.D. Khokhlova. “Elasticity mapping with high intensity focused ultrasound for prostate ablation treatment planning,” in Abstract Book of the 24th Annual International Symposium for Therapeutic Ultrasound (ISTU 2025), Banff, Alberta, Canada, 2025.

[48]G. P. L. Thomas, T. D. Khokhlova, O. A. Sapozhnikov, Y.-N. Wang, S. I. Totten, and V. A. Khokhlova, “*In Vivo* Aberration Correction for Transcutaneous HIFU Therapy Using a Multielement Array,” *IEEE Transactions on Ultrasonics, Ferroelectrics, and Frequency Control*, vol. 69, no. 10. Institute of Electrical and Electronics Engineers (IEEE), pp. 2955–2964, Oct-2022.

[49] G. P. L. Thomas *et al.*, “Phase-aberration correction for HIFU therapy 749 using a multielement array and backscattering of nonlinear pulses,” 750 *IEEE Trans. Ultrason., Ferroelectr., Freq. Control*, vol. 68, no. 4, 751 pp. 1040–1050, Apr. 2021

[50] P. B. Rosnitskiy, T. D. Khokhlova, G. R. Schade, O. A. Sapozhnikov, and V. A. Khokhlova, "Treatment Planning and Aberration Correction Algorithm for HIFU Ablation of Renal Tumors," *IEEE Transactions on Ultrasonics, Ferroelectrics, and Frequency Control*, vol. 71, no. 3. Institute of Electrical and Electronics Engineers (IEEE), pp. 341–353, Mar-2024.

[51] P. V. Yuldashev and V. A. Khokhlova, "Simulation of three-dimensional nonlinear fields of ultrasound therapeutic arrays," *Acoust. Phys*., vol. 57, no. 3, pp. 334–343, May 2011.

[52] O. V. Bessonova, V. A. Khokhlova, M. S. Canney, M. R. Bailey, and L. A. Crum, "A derating method for therapeutic applications of high intensity focused ultrasound," *Acoust. Phys*., vol. 56, no. 3, pp. 354–363, May 2010.

Pavel B. Rosnitskiy received the M.S. degree in physics and Ph.D. degree in acoustics from Moscow State University (MSU), Moscow, Russia, in 2016 and 2019, respectively. Following graduation from the Ph.D. program he was appointed as a Junior Research Scientist with the Department of Medical Physics, Physics Faculty, MSU. He is currently pursuing postdoctoral training at the Department of Medicine, University of Washington (UW), Seattle. His research interests include nonlinear acoustics, ultrasound imaging, design of multielement arrays, and therapeutic applications of high-intensity focused ultrasound waves with shocks.

Gilles P.L. Thomas received the Engineering degree in general engineering from the École Centrale de Nantes, Nantes, France, in 2014, the Engineering degree in mechatronics engineering and the M.S. degree in control and automation engineering from the Polytechnic School, University of São Paulo, São Paulo, Brazil, in 2014 and 2015, respectively, and the Ph.D. degree in biomedical engineering from the Université Lyon 1, Lyon, France, in 2019. His research interests include HIFU aberration correction, cavitation-based therapeutic ultrasound, and nonlinear acoustics.

Gerald L. Lee received the B.S. degree in biomedical engineering from the University of California, Irvine, Irvine, CA, USA, in 2023.

He is currently pursuing a Ph.D. degree in bioengineering at the University of Washington, Seattle, Seattle, WA, USA. His research interests include ultrasound imaging techniques for cavitation-based ultrasound therapy treatment planning and monitoring.

Vera A. Khokhlova received the M.S. degree in physics and the Ph.D. and D.Sc. degrees in acoustics from Lomonosov Moscow State University (MSU), Moscow, Russia, in 1986, 1991, and 2012, respectively.

After her graduation from the Ph.D. program, she was appointed by Lomonosov Moscow State University, where she is currently an Associate Professor with the Department of Acoustics, Physics Faculty. Since 1995, she has been with the Center for Industrial and Medical Ultrasound, Applied Physics Laboratory (APL), University of Washington, Seattle, WA, USA. Her research interests are in the field of nonlinear acoustics, therapeutic ultrasound including metrology and bioeffects of high intensity focused ultrasound fields, shock wave focusing, nonlinear wave propagation in inhomogeneous media, and nonlinear modeling.

Oleg A. Sapozhnikov received his M.S. degree in physics in 1985 and Ph.D. and D.Sc. degrees in acoustics in 1988 and 2008, respectively, from Moscow State University (MSU), Moscow, Russia. He is currently a Professor in the Department of Acoustics of the Physics Faculty of MSU. Since 1996, he is also affiliated with the Center for Industrial and Medical Ultrasound in the Applied Physics Laboratory at the University of Washington. His research interests are physical acoustics, nonlinear wave phenomena, medical ultrasound including shock wave lithotripsy, high intensity focused ultrasound, and ultrasound-based imaging.

George R. Schade received the bachelor's and M.D. degrees from The University of Chicago, Chicago, IL, USA, in 2003 and 2007, respectively.

He then completed his Urology residency at the University of Michigan, Ann Arbor, MI, USA, where he developed an interest in therapeutic ultrasound. Following residency, he moved to the University of Washington, Seattle, WA, USA, where he completed a Society of Urologic Oncology Fellowship and then joined the Faculty as an Assistant Professor with the Department of Urology. He is also a practicing Urologic Oncologist, aiming to develop diagnostic and therapeutic ultrasound to improve the care of patients with urologic cancers.

Kyle P. Morrison received the B.S. degree in manufacturing engineering from Western Washington University, Bellingham, WA, USA, in 2003, and the M.S. degree in medical engineering from the University of Washington, Seattle, WA, USA, in 2012. He is currently the President of Sonic Concepts, Inc., Bothell, WA, USA, where he leads its multidisciplinary engineering teams that develop premium ultrasonic transducers and systems for preclinical and clinical applications.

Francisco Chavez received a B.S. degree with ACS certification from the University of Washington in 2015, with an additional emphasis on mathematics and computer engineering. Since 2016, he has been with Sonic Concepts, Inc., Bothell, WA, USA, where he is currently the Technology Manager. In this role, he leads both the electronics and transducer design teams and has led the development of numerous ultrasonic transducers and systems that have been translated into clinical and industrial applications. His technical expertise includes ultrasound modeling, RF hardware design, and transducer design.

Tatiana D. Khokhlova received her Ph.D. degree in physics from Moscow State University (MSU), Moscow, Russia, in 2008.

After graduation from the Ph.D. program, she moved to the University of Washington (UW), Seattle, WA, USA, for postdoctoral training at the Applied Physics Laboratory. She is currently an Associate Professor of Research with the Department of Medicine, UW. Her research interests are in physical acoustics, cavitation-based therapeutic ultrasound applications and ultrasound imaging methods for therapy guidance.